CrossMark

Recycled Aluminium Alloys and their Models: Role and Behaviour of Alloying Elements during Alkaline Etching

Erlind Mysliu,[1] Kathrine Sletteberg Storli,[1] Eline Kjørsvik,[1] Otto Lunder,[2] and Andreas Erbe [1,z]

[1]*Department of Materials Science and Engineering, NTNU, Norwegian University of Science and Technology, 7491 Trondheim, Norway*
[2]*SINTEF Industry, 7465 Trondheim, Norway*

Alkaline etching is a common pretreatment for aluminum surfaces. Etching behavior was compared between an alloy based on post-consumer scrap (PCS) and several model alloys of rolled AA3005 and extruded AA6060 with systematically varied amounts of Mn, Cu and Ni. Analysis of concentrations of alloy elements in the etching solution by inductively coupled plasma mass spectrometry (ICP-MS) shows that significant fractions of the investigated elements Cu, Fe, Mg, Mn, Ni, and Zn dissolve. Surface analysis of samples in different stages of the etching process show (i) an increase in oxide layer thickness with etching time, (ii) an enrichment of important alloy elements and impurities (Cr, Cu, Fe, Mg, Mn, Si) near the metal/oxide interface, and (iii) the deposition of Mg, Fe, Si-containing aluminum hydroxide on the surface. A comparison with open circuit potential measurements and time-resolved electrochemical polarization resistance measurements enables a detailed analysis of the etching mechanism. The aluminum dissolution rate during etching is limited by the transport of species through the oxide precursor layer, thus is potential-independent. Differences in etching rates between different alloy classes, evidenced by mass loss measurements, are related to differences in the cathodic or anodic reaction mechanisms (hydrogen evolution or metal dissolution) during etching.
© 2023 The Author(s). Published on behalf of The Electrochemical Society by IOP Publishing Limited [DOI: 10.1149/1945-7111/acb38a]

Providing a composition-tolerant surface treatment is the biggest challenge toward a wide-scale implementation of recycled aluminum based on post-consumer scrap (PCS). The ability to produce recycled materials from PCS with the same properties as primary produced materials is a key step for sustainable production, as increased recycling rates for metals such as aluminum are needed.[1] Reducing dependency on critical raw materials also requires increased reuse of PCS,[2] which in turn may both require and incentivize novel business models or processes.[3] For aluminum, the remelting process adds ≈5% to the initial energy used to produce the primary aluminum, leading to an energy saving of circa 95%.[4] There are a number of further environmental and social benefits from increased PCS content in aluminum.[5,6] Both availability and demand of PCS scrap, e.g. in architectural applications, is bound to increase in the near future.[7]

Certain recycling friendly alloys can be manufactured without property loss compared to primary based alloys by adjusted composition windows.[8–12] The role of impurity elements in the adjusted composition windows of the recycling friendly alloys is far from clear. Thus, for alloys based on PCS, concerns about corrosion exist. In some cases, specific impurities can be traced to specific processing steps; for example iron impurities originate from joining processes using steel screw fasteners.[13] Some trace elements affect electrochemical properties significantly even at the ppm level, e.g. Ga,[14,15] Pb and Sn,[16] or Bi and In.[17] Approaches to manufacturing included thus production of cladded alloys with a scrap core and a primary aluminum based surface.[18] Typically, surface pretreatment is the most important step in ensuring a well protected durable surface.

Alkaline etching is one of the most common surface pretreatments performed in order to prepare aluminum surfaces for the subsequent conversion coating, anodizing or general coating application. Cleaning is also often performed under mildly alkaline conditions. Common operating conditions for the alkaline etching are aqueous solutions containing an amount of NaOH from 4 to 10 wt% with or without additives at a temperature between 40 and 90 °C.[19] The surface dissolution takes place in presence of an alumina-based film that remains on the surface throughout the

process.[20,21] On pure aluminum, these alumina films have a relatively uniform thickness and composition but their structure varies on alloys. Certain alloying elements, such as Mn, Cu, Fe, Zn, Cr, present in the bulk, tend to enrich the surface during the film formation and dissolution.[22–25] While enrichment is supposed to be eliminated by a following desmutting step,[26,27] in general, enriched alloy elements may potentially lead to initiation of localised corrosion processes later on. For this reason, studying the etching process is a good starting point to understand the evolution of the surface composition throughout the pretreatment process. Etching may also be the starting point for further modification, e.g., by hydrophobic monolayers.[28] Furthermore, etching affects the deposition of conversion coatings,[29–31] and anodisation.[21,32,33]

The aluminum dissolution mechanism under alkaline conditions for pure aluminum and different primary aluminum alloys has been studied broadly.[34–36] The first stage is usually the dissolution of the naturally formed oxide film which starts from the inevitably present defects and spreads over the whole surface.[35] The direct metal dissolution is not possible under alkaline conditions because of the thermodynamic instability of $Al^{3+}_{(aq)}$ ions at very high pH; therefore, an indirect mechanism of oxide formation and dissolution is involved.[34] For this reason, the anodic half-reaction can be described by a combination of electrochemical film formation,

$$Al + 3OH^- \longrightarrow Al(OH)_3 + 3e^- \quad [1]$$
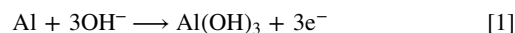
and a chemical dissolution process at the film/electrolyte interface,

$$Al(OH)_3 + OH^- \longrightarrow Al(OH)_4^-. \quad [2]$$
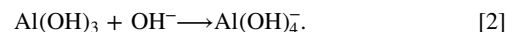
Thus, the net anodic dissolution process results from combining Eqs. 1 and 2,

$$Al + 4OH^- \longrightarrow Al(OH)_4^- + 3e^-. \quad [3]$$
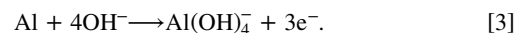
The Al^{3+} ions generated at the metal/oxide interface according to Ref. 35 by

$$Al \longrightarrow Al^{3+}_{solid\ state} + 3e^- \quad [4]$$
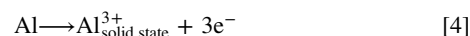
migrate across the oxide film toward the oxide/electrolyte interface where O^{2-} ions are generated.[35] These ions are responsible for

[z]E-mail: etching-recycled-al@the-passivists.org

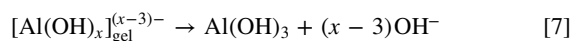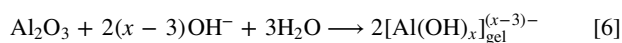**Table I. Elemental composition in wt%, as determined by optical emission spectroscopy at the manufacturers of the alloys used in this work.**

Element	3005				6060							
	Cu_HMn_L	Cu_LMn_H	Cu_LMn_L	Cu_HMn_H	Ni1	Ni3	Ni5	Ni8	Cu1	Cu4	Cu7	C1
Si	0.49	0.48	0.49	0.50	0.440	0.441	0.439	0.438	0.4271	0.4253	0.4253	0.5006
Fe	0.58	0.55	0.56	0.59	0.193	0.194	0.195	0.207	0.2319	0.2305	0.2329	0.2124
Cu	0.22	0.15	0.15	0.22	0.0010	0.0010	0.0010	0.0010	0.0005	0.0438	0.0895	0.0307
Mn	1.08	1.39	1.04	1.39	0.0517	0.0519	0.0521	0.0490	0.0571	0.0572	0.0573	0.0439
Mg	0.35	0.35	0.35	0.34	0.364	0.364	0.361	0.357	0.4730	0.4710	0.4680	0.3584
Cr	0.041	0.023	0.030	0.033	0.0006	0.0006	0.0006	0.0007	0.0011	0.0010	0.0011	0.0078
Zn	0.14	0.081	0.09	0.22	0.0006	0.0006	0.0006	0.0003	0.0289	0.0290	0.0290	0.0320
Ti	0.017	0.016	0.015	0.019	0.0151	0.0166	0.0134	0.0092	0.0133	0.0069	0.0080	0.0160
Ni	0.0305	0.0157	0.0220	0.0257	0.0028	0.0095	0.0177	0.0459	0.0040	0.0040	0.0040	0.0061
Pb	0.0095	0.0058	0.0060	0.0136	0.0011	0.0011	0.0011	0.0010	0.0010	0.0010	0.0010	0.0028

continued formation of Al_2O_3 at the metal/oxide interface,[35]

$$2Al + 3O_{solid\ state}^{2-} \rightarrow Al_2O_3 + 6e^-. \qquad [5]$$
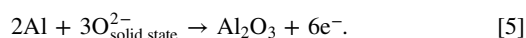
Depending on Al^{3+} concentration and pH, aluminum hydroxide precipitation may occur,[35]

$$Al_2O_3 + 2(x-3)OH^- + 3H_2O \longrightarrow 2[Al(OH)_x]_{gel}^{(x-3)-} \qquad [6]$$

$$[Al(OH)_x]_{gel}^{(x-3)-} \rightarrow Al(OH)_3 + (x-3)OH^- \qquad [7]$$

The two cathodic processes that can take place in this system are the hydrogen evolution reaction (HER)

$$2H_2O + 2e^- \longrightarrow H_2 + 2OH^- \qquad [8]$$

and the oxygen reduction reaction (ORR),

$$O_2 + 2H_2O + 4e^- \longrightarrow 4OH^-. \qquad [9]$$

The observation of gas bubbles during etching suggests that the water reduction reaction leading to hydrogen evolution is an important cathodic process.

The effect on resulting surfaces of important alloy elements and impurities such as Ni, Mg, Fe, Si during aluminum alkaline etching was investigated in some recent studies.[22–25,37,38] Nontrivial trends with composition were found when analysing the HER rates on different binary AlNi alloys after dealloying in alkaline solutions.[39] Atomic details of the surface have a large effect on, e.g., the HER rates, also on AlNi-based electrocatalysts.[40] It is in general well described that distribution of alloy elements into the intermetallic particles (IMPs), resulting from heat-treatment, affects the corrosion mechanisms and rates.[41,42] Especially in Zn-rich alloys, preferential grain etching is observed.[43] Grain etching is related to the crystallographic orientation of the grains in the surface which in turn is related to the mechanical treatment of the surface.[44] The Cu/Zn ratio critically affects the precipitation at grain boundaries, the potential distribution at the surface, and thus etching rates.[45] The exact evolution of surface composition and its effect on the electrochemical surface processes on the etching processes which occur on the second time scale is only superficially explored up to now.

The main focus of this work is to investigate, with a time resolution of seconds, if compositional variation of alloys affect the main electrochemical processes during alkaline etching. Etching of two types of aluminum alloys (rolled AA3005 and extruded AA6060) with a composition window of recycled alloys was investigated. The contents of Cu and Mn were varied for AA3005. For AA6060, two different set of samples were used and the Cu and Ni contents were systematically varied, while leaving the remaining composition constant. The etching behavior in 2.5 M NaOH solution has been investigated in situ by measurements of the open circuit potential (OCP) and by fast polarization resistance measurements during the initial phase of the etching, followed by electrochemical impedance spectroscopy (EIS) during the steady state etching. Mass loss measurements were used to complement the quantification of instantaneous etching currents. Enrichment of different alloy elements and impurities was evaluated by glow discharge optical emission spectroscopy (GD-OES), whereas the etching solutions were analysed by inductively coupled plasma mass spectrometry (ICP-MS). Surface morphology and elemental composition was assessed by scanning electron microscopy (SEM) with energy dispersive X-ray spectroscopy (EDX). The electrochemical measurements during etching were quantified by the aid of the post mortem investigation under the basic assumption that the observed OCP is a mixed potential, in line with the current paradigm in corrosion science, and that etching takes place over the full surface.

Materials and Methods

Materials.—An overview over compositions of investigated samples is given in Table I. Rolled primary-based AA3005 aluminum alloys with different Mn and Cu content were produced and provided by Speira (former Hydro Rolled Products). Manufacturing of the sheets consisted of hot rolling to 3.5 mm thickness, followed by cold rolling to a final thickness of 0.68 mm and annealing at 224 °C–230 °C. The letters "H" and "L" in the notation stand for "High" and "Low", qualitatively indicating a range of composition for Cu and Mn (example: Cu_HMn_L has a higher Cu and lower Mn content with respect to the Cu_LMn_H).

The second set of samples were primary-based AA6060 extruded alloys with systematically varied Cu and Ni content, provided by Hydro. The AA6060 samples were air cooled after extrusion and aged at 185 °C for 5 h to T6 condition. In addition, a AA6060 sample manufactured in the same way but using more than 75% of PCS is included. The received samples had not been exposed to any surface pretreatment. The samples containing 0.0005 wt%, 0.0438 wt% and 0.0895 wt% Cu will be referred to as Cu1, Cu4 and Cu7, respectively; the samples containing 0.0028 wt%, 0.0095 wt%, 0.0177 wt% and 0.0459 wt% Ni will be referred to as Ni1, Ni3, Ni5 and Ni8 respectively, and the sample made using >75% of PCS will be referred to as C1.

As the surface microstructure strongly depends on the manufacturing and will be significantly different for the rolled and extruded samples, no grinding or polishing was done here in order to compare the samples as received, which is close to a possible industrial processing. All the samples were cleaned with acetone and distilled water before each measurement.

Electrochemical experiments during etching.—The open circuit potential E_{oc} and the apparent polarization resistance R_{tot} were measured during etching in a stirred 2.5 M NaOH aqueous solution maintained at 60, 45, and 23 °C.[a] For this experiment a three electrode

---

[a]We use here a notation following the Stern-Geary equation in which the polarization resistance R_P contains only kinetics contributions, whereas the apparent polarization resistance R_{tot} is the measured quantity containing possibly more contributions; c.f. Eq. 10.

set-up was used. The working electrode was the aluminum sample under investigation, Ag |AgCl |saturated KCl (+0.197 V vs SHE) served as a reference electrode and a Pt foil was used as a counter electrode. The reference electrode was immersed in a saturated KCl solution and electrically connected to the sample cell by a salt bridge filled with Agar gel and KCl. A Gamry Reference 600 potentiostat/galvanostat was used for all the electrochemical experiments.

The etching solution was stirred and heated to the desired temperature using a lab heating plate. All the electrical connections and the experimental sequence in the potentiostat's control software were prepared before putting the working electrode in contact with the etching solution in order to start the measurement immediately after the sample immersion (≈ 1 s).

EIS measurements were conducted in 2.5 M aqueous NaOH solution at a temperature of 60, 45, 23 °C in the same cell used for E_{oc} measurements. The sample was etched for 405 s until the E_{oc} had stabilised before the EIS analysis. The frequency range was 10 MHz to 10 mHz, with an amplitude of the sinusoidal signal of 10 mV. ZSimpWin software was used for data analysis. In addition to equivalent circuit fitting presented below, an important parameter extracted from the high frequency part of the EIS measurements was the solution resistance R_s.

At selected times, the E_{oc} measurements were interrupted for a polarization resistance measurement with a scan rate of 20 mV s^{-1} in the region -5 to $+15$ mV around the initial E_{oc}. The asymmetry in the potential choice was built in as the E_{oc} during etching typically increased over time. The scan rate was chosen to achieve a sufficient time resolution and to avoid long times at an externally controlled potential. From the slope of the resulting curves, the total resistance R_{tot} was determined. Because of the fast etching, the actual polarization resistance R_P needed to be obtained from R_{tot} by subtraction of R_s,

$$R_P = R_{tot} - R_s; \qquad [10]$$

This subtraction is usually not necessary in corrosion electrochemistry because $R_P \gg R_s$, which was not the case here. The procedure here assumes a constant R_s. In particular, R_s must not be affected by different volume fractions of hydrogen bubbles.

R_P is related to the etching current density i_{etch}, the analogous quantity to the corrosion current during etching, by the Stern-Geary equation,[46]

$$
\begin{aligned}
i_{etch} &= \frac{\beta_a \beta_c}{\ln(10)(\beta_a + \beta_c)} \frac{1}{R_P} \\
&= \frac{1}{\ln(10) R_P \left(\frac{1}{\beta_a} + \frac{1}{\beta_c} \right)} \\
&= \frac{B}{R_P}.
\end{aligned}
\qquad [11]
$$

Originally derived for kinetically controlled electron transfer reactions with Tafel slopes β_a and β_c for the dominating cathodic and anodic processes, this equation is also valid for passive materials ($\beta_a \to \infty$) and transport control of the cathodic reaction ($\beta_c \to \infty$).[47] These Tafel slopes can be combined into a constant of proportionality B. Neither β_a nor β_c are a priori known for a system with fast etching such as this, and both are also difficult to measure. Therefore, the constant of proportionality B was determined experimentally for all the analyzed samples. The etching current I_{etch} was calculated from mass loss measurements (Section "Mass loss measurements") via Faraday's law using the equation

$$I_{etch} = \frac{\Delta m F z}{t M_{Al}}. \qquad [12]$$

where Δm is the measured mass loss, F the Faraday constant, M_{Al} the molar mass of aluminum, z the number of exchanged electrons

(in this case, $z = 3$) and t the time; resulting currents have been normalised with respect to surface area to obtain i_{etch}. This value and the polarization resistance value obtained from the linear polarization at steady state were used in Eq. 11 to determine the constant B. In this procedure, the effect of capacitive currents was neglected, which can easily be justified on the basis of the EIS measurements conducted at steady state.

For samples of AA3005 (Cu$_{H/L}$Mn$_{H/L}$), R_s in Eq. 10 was determined immediately after the experiment determining R_{tot} with exactly the same electrode arrangement. The determined average value of $R_s = (0.86 \pm 0.06)\ \Omega$ was used for the analysis of the other measurements, which were conducted in the same setup.

Raw data of the electrochemical experiments are available online.[48]

Post mortem characterization.—Mass loss measurements were done by immersion of samples for different periods of time (5, 15, 45, 135, 405 s) in an aqueous 2.5 M NaOH solution at 60 °C. For all the samples a fresh solution was used and all the specimens were weighed before and after the exposure to the alkaline environment and the mass loss was normalised by the sample area. Repeated preliminary experiments showed that no mass loss could be detected after the removal of the surface oxide. For this reason, no oxide removal step was conducted before weighing.

An inductively coupled plasma mass spectrometer (Agilent 8800 ICP-MS Triple Quad) was used to analyze concentrations of different ions in the etching solution. The source power was 1550 W, the plasma gas (argon flow) was 15.0 l min^{-1} and the nebulizer gas flow was 0.80 l min^{-1}. An analysis of the following elements was conducted: Al, Mg, Ti, Cr, Mn, Fe, Ni, Cu, Zn, Zr, Sn. This analysis was performed by measuring the ion concentration three times per sample. All the analysed samples were dipped in the etching solution for 120 s. The portion of solution to analyze was collected immediately after the sample exposure and diluted 100 times before the analysis. The solution was acidified using HNO$_3$; HF was added in order to avoid the precipitation of oxides or hydroxides, especially SiO$_2$. Corresponding blank samples that received the same treatment were included in the analysis.

GD-OES surface characterization was performed using a Horiba GD-Profiler 2 with argon plasma source. In order to obtain quantitative information, the instrument was calibrated with 12 different reference standards provided by MBH Analytical, Alcoa, and Alcan. The standards were chosen in order to cover the full elemental concentration range present in the alloys. Source parameters were set at 32 W applied power, argon pressure of 600 Pa. Before analysis the GD-OES source was flushed for 90 s. The sputtering depth was measured in situ using the differential interferometric profiling. Data of the GD-OES experiments are available online.[48]

SEM and EDX analysis were performed using a Hitachi S-3400N equipped with EDX. SEM images were taken using secondary electron (SE) contrast and an acceleration voltage of 15 kV.

Results

Open circuit potential and polarization resistance.—The general trend of E_{oc} evolution with time (Fig. 1) for all samples is similar, a steep increase toward more positive potential values in the beginning, usually followed by a maximum after different times, is followed by a steady state. For all the rolled alloys the maximum is reached after 60–80 s and after that, the steady state potential of each sample ranging from -1.54 to -1.51 V is reached after ≈ 130 s. The potential of sample Cu4 and sample Cu7 peaked after approximately 100 s of etching, and decreased slightly before reaching relatively steady values between -1.65 V and -1.61 V after 175 s. Sample Cu1 reached a stable potential after ≈ 40 s. The magnitude of the stable E_{oc} also follows a common trend. For AA3005, E_{oc} is shifted toward more positive values passing from low to high Cu and Mn content (Fig. 1a). Analogously, for AA6060, the E_{oc} increases with
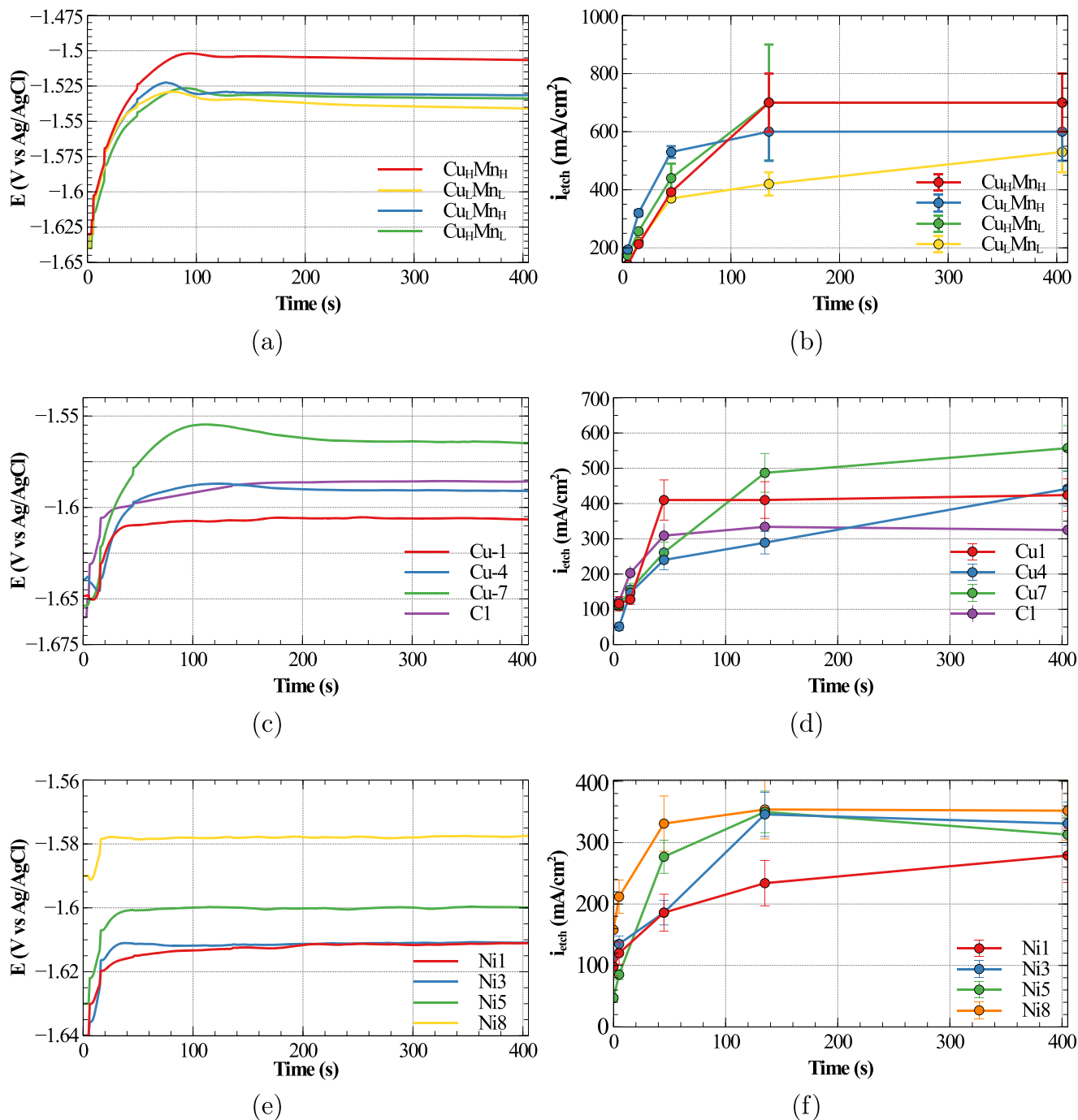
Figure 1. E_{oc} (a), (c), (e) and etching current density i_{etch} (b), (d), (f) of AA3005 and of AA6060, respectively, measured during etching in 2.5 M NaOH at 60 °C.

increasing Cu or Ni content (Figs. 1c, 1e). Qualitatively similar trends are observed for i_{etch} (Figs. 1b, 1d, 1f), which were obtained based on the analysis described above, in Section "Electrochemical experiments during etching", The reaction rate for all the investigated samples increased very rapidly in the beginning and reached a stable value after 120 s. The mass loss Δm for all the investigated samples measured after 5, 15, 45, 135, and 405 s of exposure to the etching solution is reported in the Supplementary Material, SM-Section 3. As an example, Δm for sample $Cu_H Mn_L$ is presented in Fig. 2. Comparing these data to E_{oc} measurements shows that a stable E_{oc} is reached after the dissolution of $d \approx 27$ μm of metal. Based on the calibration data in Fig. 2, the thickness d was estimated by $d \simeq \frac{\Delta m}{\rho}$, assuming that the etching process proceeds homogeneously over the whole surface.

Effect of temperature on etching electrochemistry.—The effect of temperature on etching was investigated by monitoring E_{oc} of $Cu_H Mn_L$ during etching at different temperatures. The shape of E_{oc} with time is similar at all the tested temperatures. However, the stable E_{oc} is reached in a shorter time with increasing temperature (Fig. 3a).

The activation energy E_a of the etching process was calculated from the Arrhenius equation,[49] $\ln(i_{etch}) = \ln(A) - \frac{E_a}{RT}$, where A is a constant, T the absolute temperature and R the universal gas constant, using the data in Fig. 3b. The Arrhenius plot is presented in Fig. 3c.

The slope of the line in Fig. 3c was used to estimate an activation energy of (17 ± 4) kJ mol^{-1}. This value is of the same order of magnitude as reported by different authors for aluminum dissolution near OCP for similar systems,[50–57] though with different alloy compositions.
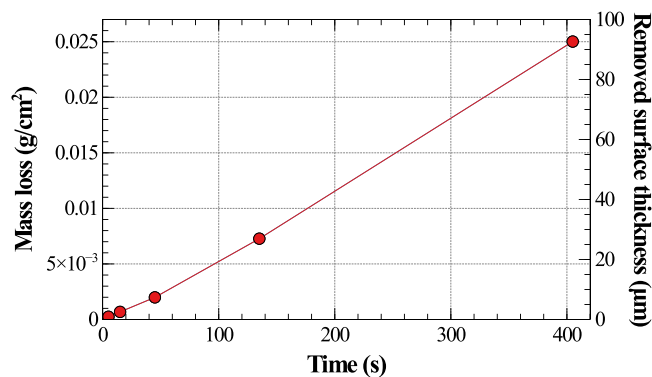
Figure 2. Mass loss and corresponding removed surface thickness assuming uniform etching after 5, 15, 45, 135, and 405 s.

Electrochemical impedance spectroscopy.—The Nyquist plots (Fig. 4) of Cu_HMn_L AA3005 in 2.5 M NaOH consist of a large semicircle at high frequency followed by a smaller semicircle and a very small inductive loop at intermediate frequency which is difficult to visualise, and a capacitive loop at lowest frequencies. Some similar impedance plot have been reported in literature for aluminum alloys exposed to different solutions.[51,58–63] However, all the previous authors report only one semicircle in the high frequency region for the investigated aluminum alloys. An interpretation of the different elements is discussed in SM-Section 5.

Semicircles become larger with decreasing temperature (Fig. 4), especially when comparing 45 °C to room temperature. Increasing semicircle diameter could be attributed to both an increase of the oxide precursor layer[b] thickness because of a decreased solubility, or a reduced electrochemical reaction rate with decreasing temperature. In both cases the etching rate is lower at lower temperatures (Fig. 3b).

Based on the understanding outlined in the introduction, a simplified model can be used to justify the equivalent circuit used for fitting Fig. 4. The oxide precursor layer on aluminum in strongly alkaline solution consists of an inner and an outer oxide layer.[64] In the model presented here, R1 is associated with the charge transfer resistance of aluminum dissolution, and C1 is associated with the double layer capacitance present at the interface. The RL parallel accounts for the adsorption of anions on the outer layer,[65] while the C2 and R4 elements are, respectively, the capacitance and resistance of the inner layer. R2 accounts for the transport of species through the two surface layers and the constant phase element (CPE) is used to model the capacitance of the two (inner and outer) oxide layers. The low frequency resistance from EIS agrees typically within ca. 10% to R_{tot}, Eq. 10. In modulus plots, the low frequency and high frequency values are on the same order of magnitude, which makes the correction described in Eq. 10 necessary.

The low frequency capacitive loop (described by C2 and R4 in Fig. 4d) is evident at 60 °C and 45 °C, but it decreases in prominence at 23 °C. A possible interpretation of the differences between room and higher temperatures is that the oxide precursor layer at room temperature has a higher thickness because of its reduced solubility. Higher thickness would lead to a lower electric current through the layer compared to higher temperatures. Post-mortem evidence for the presence of hydroxide comes from the infrared spectrum of the layer, Supplementary Material, SM-Section 6.

Surface analysis.— *GD-OES.*—For Cu_HMn_L, the etching process was followed also by GD-OES after 5, 15, 45, 135, and 405 s of immersion in the etching solution. The GD-OES analysis in Fig. 5 shows that the quantity of many elements is higher near the surface. All of them follow a similar trend of enrichment in the region between 0.01 and 0.1 μm for the first 15 s. After 45 s there is a small
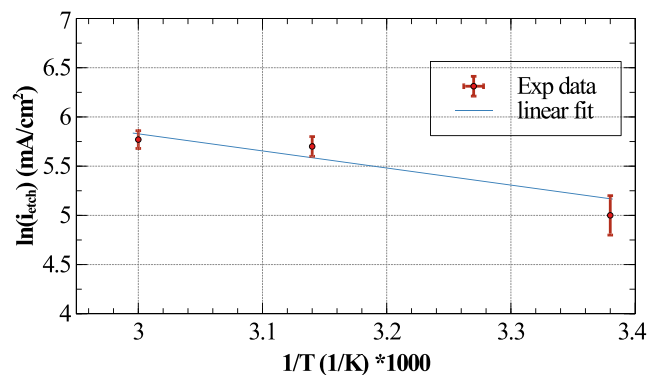
[b]We use the term "oxide precursor layer" here for the surface layer present in solution, which contains likely also solvated species and develops into the hydroxide film containing residual alloy elements, the "smut" layer, after removal from the etching bath.
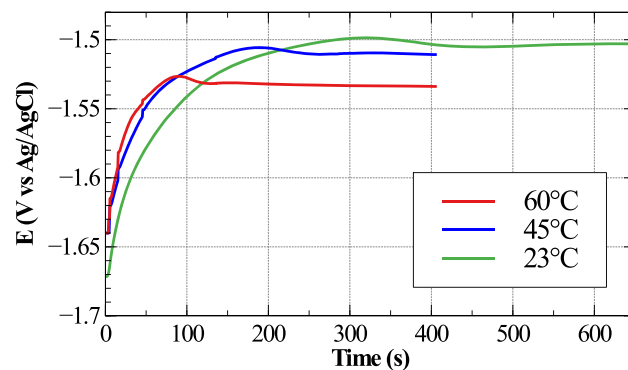
(a)
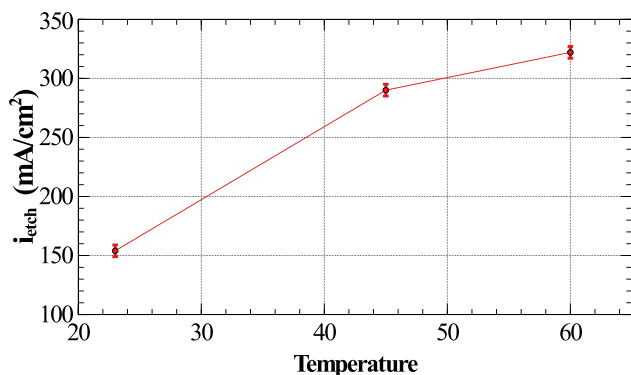
(b)

(c)

Figure 3. Effect of temperature on OCP (a), and etching current density (b); Arrhenius plot for etching (c). Sample: Cu_HMn_L AA3005 in 2.5 M NaOH.

depletion in this region and an enrichment in the region between 0.1 and 1 μm reaching a value that remains stable after 135 and 405 s of immersion (Fig. 5). The trend is very similar for all the elements except for Mg which shows a small enrichment also before etching (0 s). It is worth noting that the time after which a non-changing element enrichment is observed agrees well with the time needed by the same system to reach a stable E_{oc} and i_{etch}.

Further information is obtained from an analysis of the aluminum and oxygen profiles. An enrichment of all the elements takes place also in the (hydr)oxide layer which grows during the first period of etching until reaching a stable value after ≈120–130 s (Supplementary Material, SM-Section 2). Even though for oxygen an absolute quantitative information is not present due to lack of standards, it is worth analysing the shape of its depth profile. If the crossing point of the aluminum and oxygen profile is plotted against the exposure time
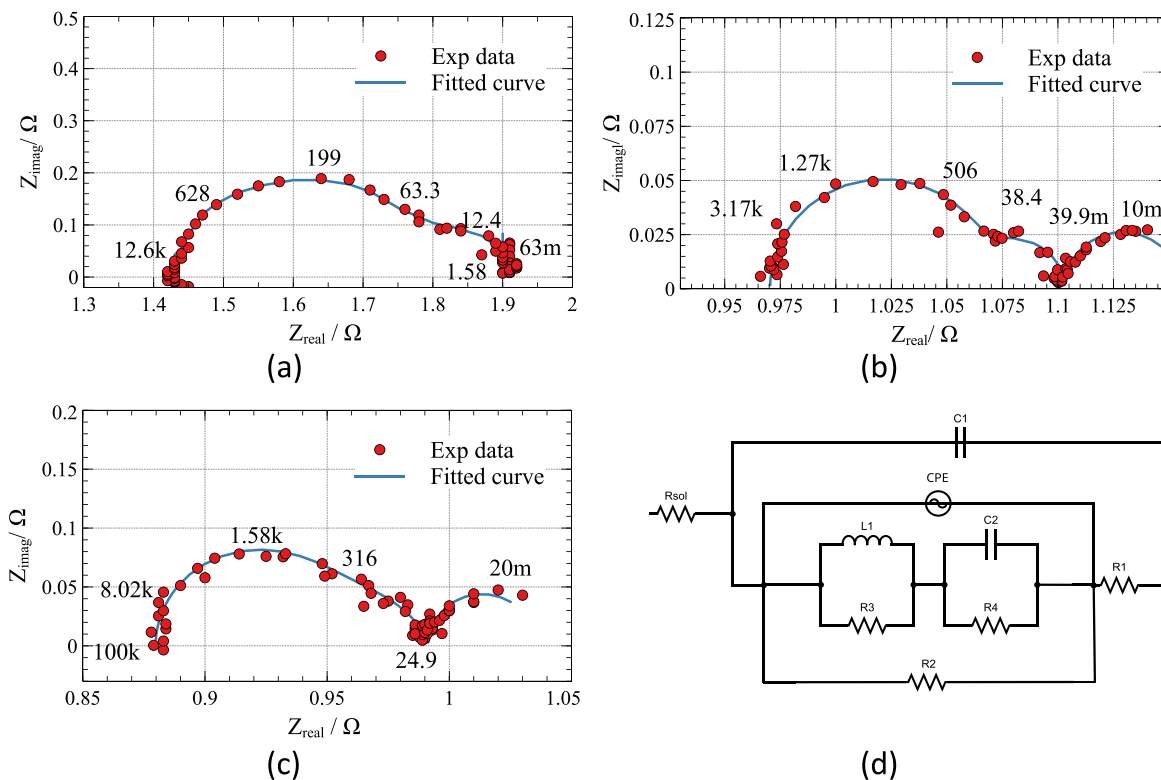
Figure 4. Nyquist plot for Cu_HMn_L sample at different etching bath temperatures, 23 °C (a), 45 °C (b), 60 °C (c) and equivalent circuit used for data fitting including an approximate justification based on a simplified structural model (d); one capacitive element could not be described by a pure capacitance and a constant phase element CPE was introduced instead. The fitting parameters are compiled in SM-Table II. Evidence for the presence of hydroxide comes from the infrared spectrum of the layer (SM-Fig. 11).

(Fig. 6), the obtained curve closely follows the trends already observed from E_{oc} and i_{etch} evolution (Fig. 1). This trend is independent of the calibration factor that would be used for the oxygen signal.

Scanning electron microscopy.—After etching, from a morphological point of view (Fig. 7) all surfaces are similar and they are characterized by the presence of craters and bright particles with a variable geometry.

Representative EDX mappings of one sample are shown in Fig. 8. A comprehensive collection of images and EDX maps for other investigated samples is found in the Supplementary Material, SM-Section 1. Detailed characterization of the surface microstructure of very similar alloys has been reported elsewhere.[66–70] EDX mapping showed a colocation of bright spots with comparatively large intensities of Mn, Fe and Si, for all the investigated AA3005

samples. Thus, the composition of the bright particles is mainly Al (MnFe)Si. A more comprehensive characterization of these specific IMPs has been reported.[70] The quantity of Cu and Zn is lower in Cu_LMn_L and these elements are almost absent in Cu_LMn_H. For Cu_HMn_L, the presence of magnesium (hydr)oxide, manganese oxide and iron oxide was inferred from the colocation of oxygen rich areas with magnesium, manganese and iron rich areas.

ICP-MS.—Quantitative analysis by ICP-MS of the etching electrolyte after etching is compiled in Table II. In all investigated alloys, significant concentrations of the noble elements Cu and Ni were found; besides the relatively high background for Ni, there is clearly a higher Ni concentration than expected for congruent alloy dissolution for Ni8. Also Fe and Mn dissolve from the alloy; for Zn, the large background concentration makes a quantification difficult

Table II. Concentration of different elements in the etching NaOH solution, in $\mu g/l$, from ICP-MS analysis of etching solutions of three different samples as indicated; meas.—experimentally determined concentration; SD—standard deviation in % from three measurements of the same sample; calc.—calculated concentration from experimentally determined mass loss Δm assuming equal dissolution of all alloy elements, via $\frac{\Delta mA}{V} dw$ where A is the sample area exposed to a volume V of the etching solution, w is the amount of alloy element present in the sample in wt% and d is the dilution factor (Section "Post mortem characterization"). SD values do not reflect deviations between different samples. For Ti, Cr, Zr, and Sn, no increased concentrations above the background values were found. Si could not be analysed due to a large background, presumably from vials. The full dataset is available with the raw data package.[48] Background concentrations in blank samples are shown in the Supporting Material, SM-Section 4.

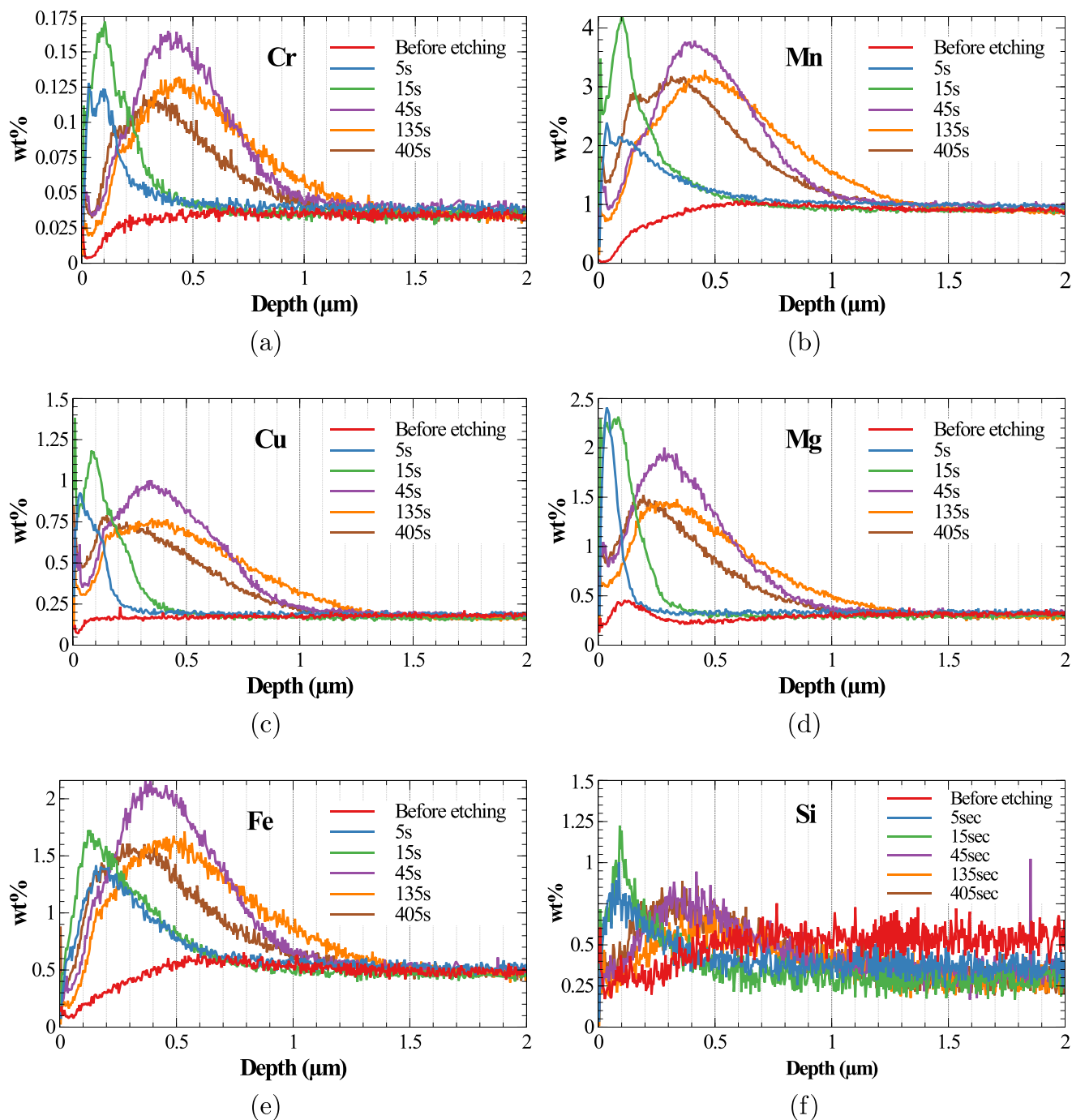|	Cu_HMn_L				Ni8				Cu7			
	meas.	SD	calc.	ratio	meas.	SD	calc.	ratio	meas.	SD	calc.	ratio
Mg	5.56	1.1	8.77	0.63	19.7	1.4	15.93	1.24	7.7	0.9	28.72	0.27
Mn	17.8	0.4	27.07	0.66	2.79	1.2	2.19	1.27	1.15	0.5	3.52	0.33
Fe	12.1	0.1	14.54	0.83	14.8	1.2	9.24	1.60	8.48	1.0	14.29	0.59
Ni	0.84	4.5	0.76	1.10	2.98	4.3	2.05	1.45	0.75	8.9	0.25	3.00
Cu	3.26	3.8	5.51	0.59	0.39	8.8	0.045	8.67	1.1	2.8	5.49	0.20
Zn	2.22	3.6	3.51	0.63	0.23	4.0	0.013	17.69	0.79	9.0	1.78	0.44

Figure 5. GD-OES profile for Cr (a), Mn (b), Cu (c), Mg (d), Fe (e), and Si (f) for Cu_HMn_L after etching in 2.5 M NaOH at 60 °C for the specified period of time.

except for sample Cu_HMn_L. The most active element Mg, which also forms an insoluble oxide under the conditions present here, shows sometimes an increased dissolution (Ni8), but for Cu7 a decreased dissolution compared to the remaining alloy.

Discussion: Surface Enrichment of Alloy Elements and Effect on Electrochemical Properties During Etching

The surface morphology after etching of the different rolled samples is very similar, judged from SEM images. The GD-OES analysis conducted on rolled samples after different etching times shows that an oxide/hydroxide layer is growing for ca. 100 s, reaching a constant thickness afterwards. The comparison of the elemental

depth profile presented in Figs. 5 and 6 shows a pronounced enrichment of Cu, Mn, Cr and Fe both on the metal side of the metal/oxide interface and in the oxide. All these metals are nobler than aluminum and may thus cause the preferential dissolution of the adjacent aluminum matrix. An exception is that of Mg that showed a small surface enrichment also before exposing the sample to the alkaline solution and that could be attributed to the presence of Mg rich oxide islands.[71] (While it is understood that different sputtering rates in the GD-OES can produce erroneous results, enrichment would only be expected under certain very special circumstances that lead to uneven depth distribution of IMPs laterally).

For pure aluminum the observed increase in E_{oc} during etching has been attributed to the oxide layer growth,[34] whereas in the case
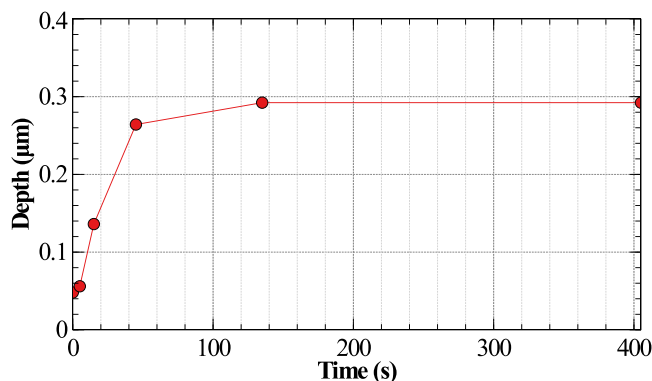
Figure 6. Estimated oxide thickness during etching (crossing point of the aluminum and oxygen profile) for different etching times. Corresponding profiles in Supplementary Material, SM-Section 2.

of aluminum alloys, the increase is also related to the presence of alloying elements.[35] The generally observed initial reduction of E_{oc} in the first 5–10 s of etching (Fig. 1; in this study observed only for the AA6060 extruded alloys) was previously attributed to alumina film dissolution,[35] and the results from this work do not contradict this interpretation. The subsequent increase in E_{oc} up to ≈100 s can be explained by ongoing aluminum dissolution. An increase in concentration $[Al^{3+}]$ corresponds to an increase in reversible potential E^{rev} according to the Nernst equation for aluminum dissolution,[49]

$$E^{rev} = E'_0 + \frac{0.059V}{3} \log_{10}[Al^{3+}]. \quad [13]$$

During this phase, an enrichment in alloy elements at the the metal/oxide interface occurs; this enrichment is not required to explain the E_{oc} evolution, though enrichment may influence the observed trend.

The steady state value of E_{oc} reached after more than ≈150 s for most samples is governed by the enrichment of alloy elements at the surface, because of the observed direct correspondence between the potential value and the amount of alloying elements, as detected by GD-OES. The maximum detected surface concentration by GD-OES is increasing with increasing amount of Cu and Ni (Supplementary Material, SM-Fig. 6) for the respective sample series.

The increase with time of i_{etch} (decrease of R_P) suggests that the system becomes more reactive during the first 50–100 s, probably because of the emergence of IMPs causing a higher cathodic activity and increasing HER rate. A larger fraction of the surface covered with a material with low R_P, such as a cathodically active intermetallic particle, is expected to lead to an overall decrease of the net R_P of the entire surface. After 120–130 s and 50 s, respectively, a more stable etching rate is reached for AA3005 and AA6060. The time to achieve a stable etching current corresponds well with time to a relatively stable E_{oc}. Previous studies[35] showed that a reduction in stable E_{oc} value indicates a decreased availability of cathodic sites available for HER; such sites are typically secondary phase particles. Figure 1 shows some correlation between the nobility of a surface (E_{oc}) and the etching current (i_{etch}), which would be expected. There is, however, no obvious functional correspondence between the two quantities.

Based on the considerations in the previous paragraph, the internal structure of the developing "smut" layer, i.e. the oxide-rich and alloy element rich layer on the aluminum surface, must play an important role. The dissolution rate of different particles in alkaline NaOH solution varies considerably.[72] Si containing particles such as α-AlFeSi, α-AlFeCuSi, α-AlFeMnSi dissolve slower than the matrix, while Al_3Fe, Al_6(Mn, Fe), Al_6(Mn, Cu) and Al_6Mn dissolve at similar or higher rates with respect to the matrix.[72] The dissolution rate of these particles must be a very sensitive function of

the actual surface composition, i.e. how well the constantly changing surface catalyses the HER. Indeed, a series of recent studies[23–25] demonstrated that the cathodic activity of different IMPs could vary as a consequence of their partial anodic dissolution resulting in formation of a surface film with different morphology and composition on the different IMPs. Thus, the deposition of a somewhat porous film on the particle surface leads to a time dependent electrochemical reactivity of IMPs during exposure to an alkaline solution.[23,24] A coverage of IMPs with oxides is also observed here by SEM/EDX, and is consistent with the observed GD-OES data. The deposition of etching products on IMPs could be correlated with the presence of the "knee" observed on the E_{oc} profile. Indeed, the shift of the element enrichment shown in Fig. 5, is observed after the same amount of time required to reach (and overtake) the "knee".

As shown by the ICP-MS measurements, there is substantial amount of dissolution of the alloy elements Cu, Fe and Mn. These elements are expected to redeposit in contact with an active metallic aluminum surface. However, the high amount of elements found in solution suggests that the redeposition might be hindered by the growing (hydr)oxide layer. The measurement in solution of significant concentrations of these elements which in pure phase are more noble than aluminum indicates that during the fast etching process that occurs here, there is very little protection by galvanic coupling of these more noble elements with the matrix. The overall amount of dissolved alloy elements cannot easily be explained with a dissolution of IMPs alone, which should however significantly contribute to the detected amounts via dealloying processes.[73–75] Iron and manganese oxides are detected on the location of the IMP. Thus, there is deposition of some of the alloy elements in the form of oxides on the surface of the IMP. A recent study provides similar evidence for the dissolution of noble alloy elements during acid etching.[76]

Detachment of IMPs during the dissolution process is likely happening, but cannot be proven or disproven by the data collected here. Release of particles has been deduced from concentration spikes in, e.g., Cu from in situ downstream concentration determination by atomic emission spectroscopy during alkaline etching,[77,78] or by rotating ring disk electrode.[74] Such detachment can affect the detected concentration of alloy elements by ICP-MS. Release of alloy elements can also occur via dealloying of IMPs.[73–75] Remnants of detached dealloyed IMPs have in 2xxx alloys been suggested to contribute to non-Faradaic Cu release.[73,74]

Quantitatively, using Fe as indicator element for IMPs, an analysis of EDX maps shows areas of 5%–6% covered by IMPs, leading to the reasoning the the volume fraction must be on the same order of magnitude. Because of the higher density of IMPs, the mass fraction should be slightly higher. The analysis of i_{etch} conducted below based on the mass loss measurements would be affected by the non-Faradaic process of detachment. However, this error would be on the order of 10%, and thus on the order of the statistical uncertainty of the obtained Tafel slopes, based on the total mass of IMPs on the alloy. We reason therefore that the overall mass loss is only to a minor degree affected by detachment or dealloying of IMPs, and the systematic error on the Tafel slopes is not changing any of the quantitative conclusions drawn below.

The surface enrichment of Cu, Fe, and Mn on the metal side of the metal/oxide interface and the growing oxide precursor layer with etching time lets us reason that the transport of these alloy elements into the solution must occur through the oxide precursor layer. Also other studies found enrichment of Zn,[79,80] and Cu[32,81] on the metal side of the metal/oxide interface. Furthermore, the presence of an enrichment of Cu, Mn, Cr and Fe on the oxide side of the metal/oxide interface can be because of either the redeposition of these elements from the etching solution, or their transport through the oxide precursor layer. For most alloy elements which are more noble than Al, the observed concentration ratio still indicates a preferential dissolution of Al. Exceptions may be related to the concentration ratio in IMPs and metal matrix, and the differences in dissolution kinetics between the two.
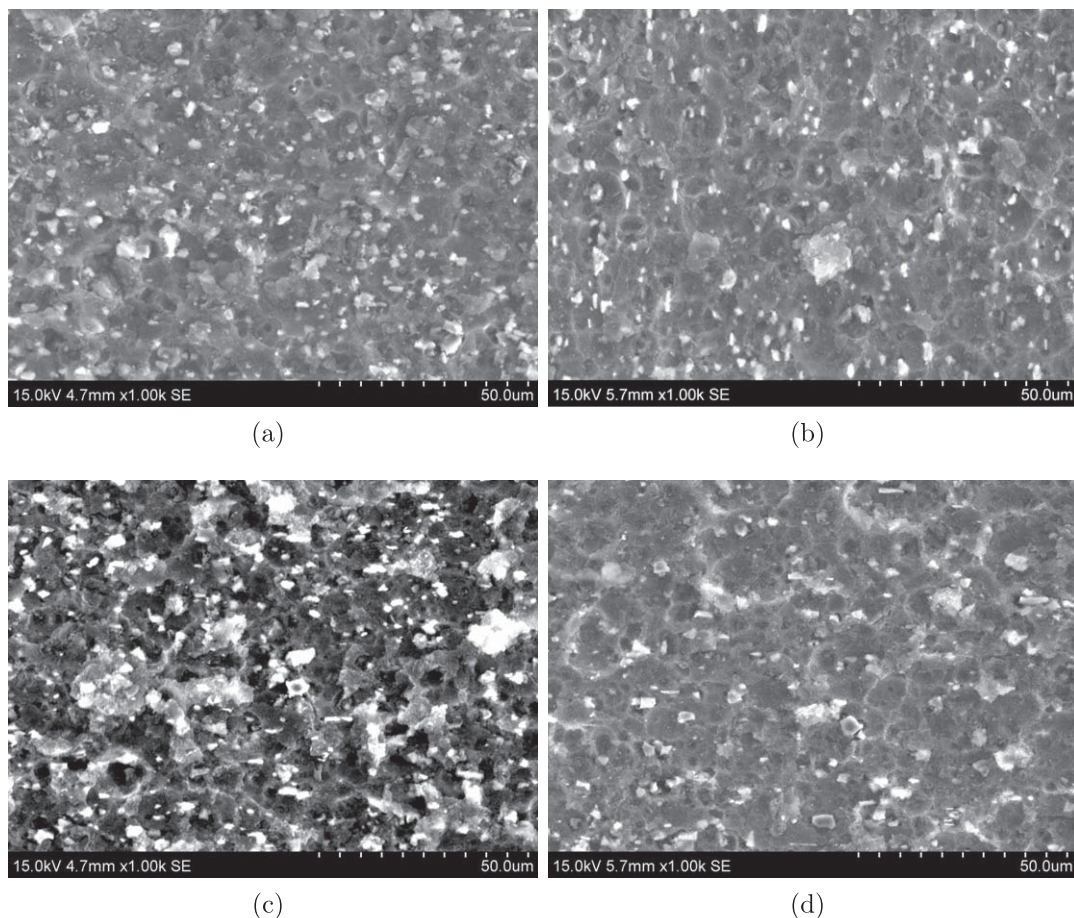
Figure 7. Secondary electron images on AA3005 of Cu_HMn_H (a), Cu_LMn_H (b), Cu_HMn_L (c), Cu_LMn_L (d) after alkaline etching in 2.5 M NaOH solution at 60 °C.

The experimentally determined value of $B \approx 0.03...0.15$ V, with typically 10% uncertainty, indicates both an oxide-covered surface in situ as well as higher Tafel slopes than usual for both anodic and cathodic reactions; these values could imply some form of transport control of anodic metal dissolution or cathodic hydrogen evolution. Typical textbook values of B for activation controlled processes are 0.026 V or 0.022 V,[82] i.e. values that are mostly lower than the experimentally determined values. At 60 °C, these value would become 0.029 V. For kinetically controlled reactions, Tafel slopes are typically on the order of 30–120 mV dec^{-1}. It is straightforward to verify from Eq. 11, e.g. the form in the second line, that if one of the Tafel slopes approaches infinity (indicating transport control or passivity), while the other is 30–120 mV dec^{-1}, the value of B would be 0.01...0.05 V. For only two measured samples the results lie on the upper end of this interval, while most samples show higher values of B. Thus, both anodic and cathodic Tafel slopes must be higher than 120 mV dec^{-1}. This reasoning is based on the assumptions that (i) matrix dissolution is an electrochemical process, (ii) dissolution fluctuates all over the surface and is approximately equally fast on lateral average, (iii) dissolution of the matrix dominates.

Literature reports on Tafel slope measurements under conditions resembling those present here support such a reasoning. Tafel slopes for the anodic aluminum dissolution of 225 mV dec^{-1} and for the cathodic hydrogen evolution of 170–300 mV dec^{-1} were found; when the electrode was negatively polarized, a large amount of hydrogen bubbles were evolving from the surface leading to a situation in which the kinetics was dominated by the Ohmic drop for the aluminum dissolution in 4 M NaOH.[83] In a study of aluminum dissolution in KOH, the rate of both cathodic and anodic reactions were almost independent of the electrode potential, indicating Tafel slopes approaching infinity.[84] A Tafel slope of ≈ 600 mV dec^{-1} was found for aluminum dissolution in up to 7 M KOH.[50] Tafel slopes ranging between 180 and 240 mV dec^{-1} for hydrogen evolution on oxide-covered aluminum were observed.[85] Also a study combining EIS with downstream electrolyte analysis during alkaline etching of AlZn found that under cathodic currents, the dissolution of aluminum was potential independent,[86] corresponding to a high Tafel slope as must be present here. In this work, the obtained B can either be explained by both Tafel slopes being slightly higher than the literature values, or by one Tafel slope approaching infinity and the other one lying on the upper end of the previously observed interval. While a more detailed discussion of B requires more sophisticated electrochemical studies, some conclusions can be drawn from the comparison of the samples here.

The different values for B in the different sample classes (Supplementary Materials, SM-Section 3) indicate a change in mechanism in one of the involved electrochemical reactions as function of alloy composition, and not a difference in available surface area of cathodic IMPs. When comparing the data for B for the three samples series, the values from the copper series (Cu1, Cu4, Cu7) are significantly higher than the other two series. Likewise, the samples of the nickel series (Ni1, Ni3, Ni5, Ni8) show with one exception the lowest B in this work. There is almost one order of magnitude difference between the lowest and the highest B observed here. As the value of B basically comprises Tafel slopes depending on the reaction mechanism or rate-controlling processes, these differences must be reflected in differences in the mechanism. In particular, there is no systematic dependence of R_P on the alloy composition; therefore, we can rule out a systematic
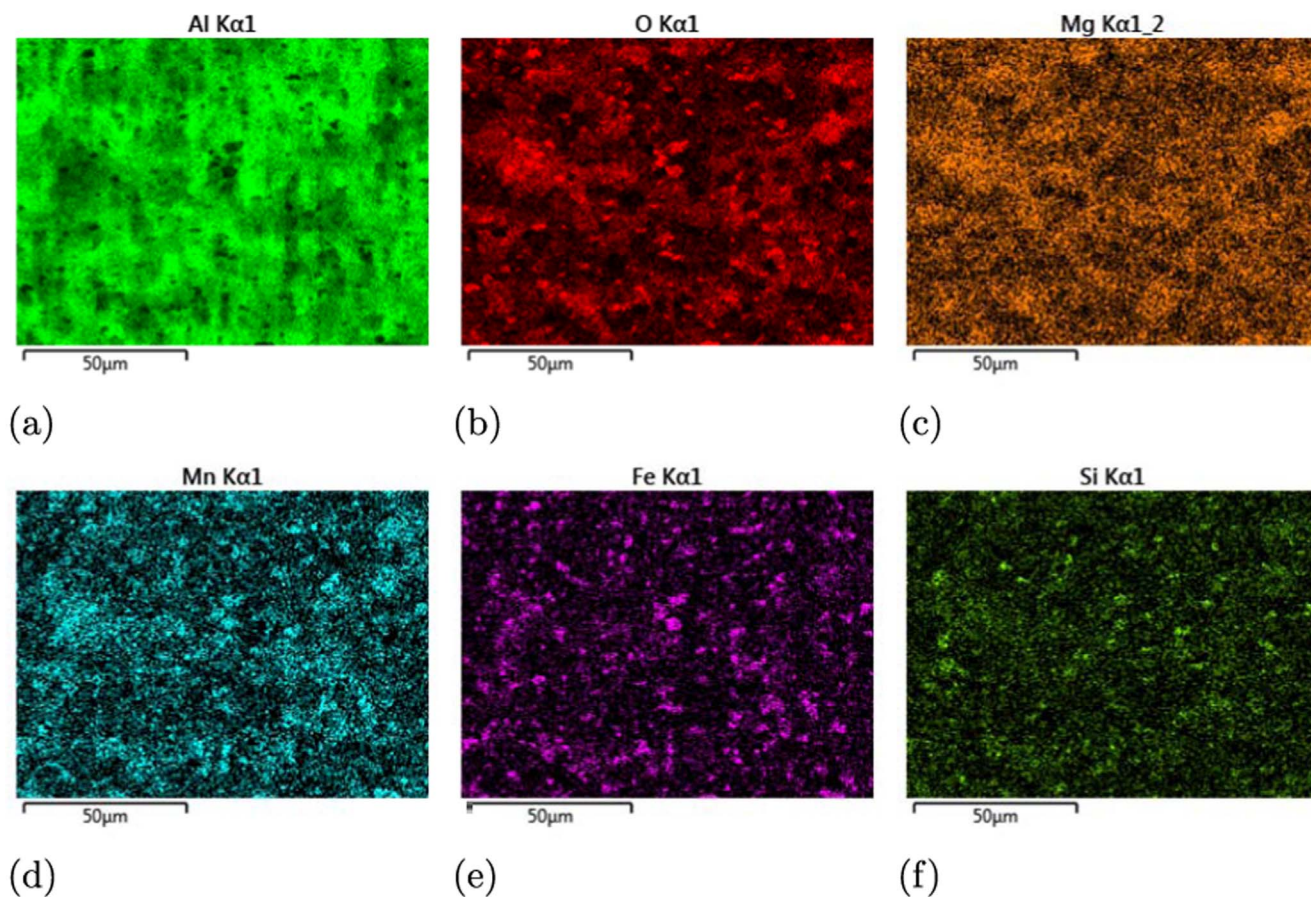
Figure 8. EDX mapping on $Cu_H Mn_L$ of Al (a), O (b), Mg (c), Mn (d), Fe (e), Si (f) after alkaline etching in 2.5 M NaOH solution at 60 °C.

difference in cathodically active surface area between the samples, despite significant (order of magnitude) variation in the content of copper and nickel in the respective sample series. It was recently argued that differences in the population density of IMPs alone can account for the different etching rates of two 5xxx alloy;[25] the results from this work imply that for the alloys studied here, there are further differences between the surfaces. The variation in *B* may still be related to changes of, e.g., HER mechanism because of different surface composition of IMPs in the different alloys. Such changes may be expected as IMPs over time cover with different own oxidation products.[23,24,72] Alternatively, an effect on aluminum dissolution cannot be ruled out on the basis of the data here.

The activation energy for etching of (17 ± 4) kJ mol^{-1} found during this work is in agreement with the activation energy for aluminum dissolution in alkaline conditions observed previously.[52–56] This value has been reported to be between 10.76 and 68.4 kJ mol^{-1}. The observed activation energy is too low to be associated with typical covalent bond formation or breaking, and too low to be associated with the oxygen lattice diffusion in aluminum oxide.[87,88] Activation energies between 10 and 100 kJ mol^{-1} could be associated with different hydrogen bonds, suggesting a mechanism of transport of hydroxide ions to the aluminum surface.[52] This activation energy is also in the same order of magnitude as the viscous flow in water, (15.8 ± 0.3) kJ mol^{-1} based on values in Ref. [89] which determines the activation energy of diffusion in aqueous solution, as can be rationalised e.g. by the Stokes-Einstein equation. Aleksandrov et al.[52] assume a mechanism in which the first step of aluminum dissolution is the chemisorption of two hydroxide ions on hydrated aluminum atoms with the chemisorption of the second hydroxide ion being the rate determining step. The negative activation entropy values for the aluminum dissolution in alkaline media found in previous works[62] has been interpreted such that this process should be an association

process rather than a dissociation.[52] In aqueous solution, entropies are, however, strongly affected by effects on the water network through the hydrophobic effect, which is also temperature dependent and has thus non trivial consequences that would need a deeper study, as e.g. available in soft matter systems.[90] As an alternative to a previous interpretation,[52] the transport of species through a strongly hydrated oxide precursor layer appears reasonable from the results of this work. The observed correlation between etching current and the thickness of the dried oxide layer in post mortem analysis, (Figs. 1 and 6) and the high Tafel slopes needed to explain *B* are strong indications that current is limited by transport through this oxide precursor layer. The observed activation energy is also consistent with this interpretation.

The suggested etching mechanism in line with the discussion above is summarised in Fig. 9. Initially (Fig. 9a), the surface is covered with an magnesium-containing aluminum oxide. Etching phase 1 starts with a removal of the aluminum oxide on the surface in the first seconds of the process (Fig. 9b). The result is an active surface, with fastly dissolving aluminum (phase 2). In this phase, non-Faradaic particle detachment may occur, which can neither be concluded or ruled out from this work, but was evidenced in literature works.[77,78] Also, locally, the aluminum concentration will be high enough to reach the solubility product of an oxide precursor, which may happen practically instantaneous so that direct oxide formation occurs. The result is a growing aluminum oxide precursor layer, and an increased availability of IMPs on the surface (Fig. 9c). IMPs will possibly detach and also dissolve, but necessarily at different rates than the aluminum; both the remains of the IMPs and their dissolution products will become part of the growing oxide precursor layer. After ≈ 100 s depending on the exact alloy, a steady state (phase 3) is reached in which the dissolution rate of the oxide precursor layer and the reformation rate become equal (Fig. 9d). The amount of available cathodic sites remains almost
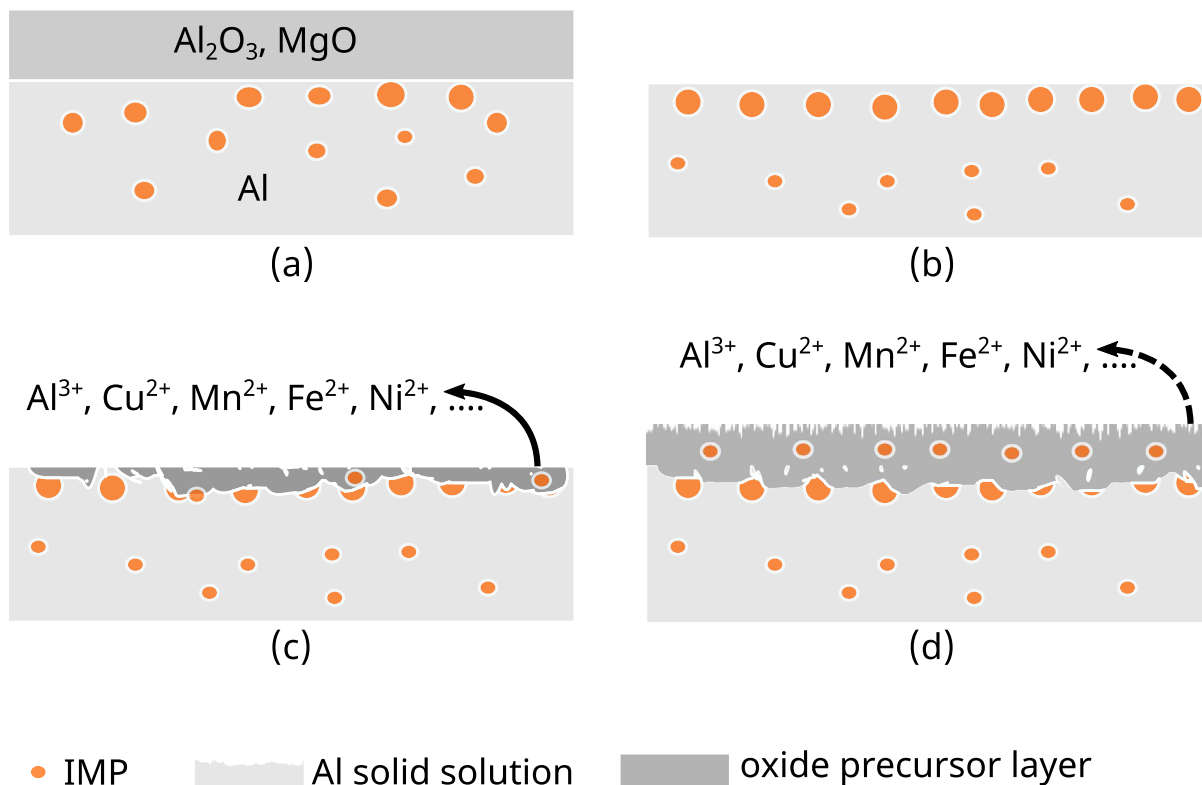
Figure 9. Suggested etching mechanism.

constant in the phase 2 and phase 3. Catalytic activity of the surface does not change much during etching, however, cathodic activity depends on the alloy composition, via different etching mechanisms. The nature of the differences between mechanisms of electrochemical process on the different alloys is yet to be revealed.

Conclusions

The behavior during alkaline etching of recycling friendly rolled AA3005 and extruded AA6060 aluminum model alloys was studied, and compared to an alloy based on more than 75% PCS corresponding to AA6060. In situ electrochemical measurements of open circuit potential and etching current during the etching process show no characteristic differences between primary based and recycled alloys. The increase of open circuit potential and etching current with time is consistent with the well established increase in cathodically active surface area during etching by exposing IMPs. GD-OES measurements show the enrichment of noble surface elements during the etching process.

A more surprising result of this study is the fact that the etching current differences between different alloys can be traced to differences in the electrochemical reactions mechanisms on the different alloys, instead of being related to a difference in the area of cathodically active IMPs or noble dissolution residues. ICP-MS analysis confirms the presence of all investigated alloy elements (Cu, Fe, Mn, Mg, Ni) in the etching solution; significant fractions (typically more than 50%) of noble alloy elements dissolve, indicating that the dealloying of the surfaces also involves dissolution of the noble alloy elements. Consequently, a redeposition of noble elements is possible if active aluminum surface is present. Nevertheless, the high concentration found for the different elements suggests that the redeposition might be partly hindered by the presence of the oxide precursor layer in solution. Migration of Al^{3+}, OH^- and O^{2-} ions ensure a continuous formation of Al_2O_3, $AlOOH$ or $Al(OH)_3$ at the film/alloy interface, consistent with EIS data during steady state etching. Alloy elements also enrich at the oxide/metal interface, as evidenced by GD-OES. GD-OES depth profiles also hint to the presence of an oxide precursor layer, via the change in the intersection

of the Al/O concentration. In addition to aluminum (hydr)oxides, (hydr)oxides containing Al, Mg, Fe and Si deposit on the surface.

The thickness of the "smut" layer, comprising of aluminum (hydr)oxides and alloy elements diminishes with increasing temperature due to the enhanced solubility of aluminate ions, as concluded from interpretation of EIS data. Considering (i) the etching current increase with increasing temperature, (ii) the activation energy consistent with diffusion processes in aqueous solutions and (iii) the magnitude of the *B* constant of the Stern-Geary equation, it can be concluded that aluminum dissolution during etching is limited by the transport of species through the oxide precursor layer.

The complex interplay of the different simultaneous processes of aluminum dissolution, emergence and dissolution of IMPs, deposition and dissolution of the "smut" layer, and hydrogen evolution, shows no evident difference when comparing an aluminum alloy based on post-consumer scrap with primary-based model alloys.

ORCID

Andreas Erbe https://orcid.org/0000-0002-7777-2258

References

1. L. Akenji et al., *Sustainable Consumption and Production* (Nairobi, Kenya)(United Nations Environment Programme), p. 25 (2015), https://sdgs.un.org/sites/default/files/publications/1951Sustainable%20Consumption.pdf.
2. G. Gaustad, M. Krystofik, M. Bustamante, and K. Badami, *Resour. Conserv. Recycl.*, **135**, 24 (2018).

3. K. Martinsen and S. Gulbrandsen-Dahl, *Proc. CIRP*, **29**, 686 (2015).
4. European Aluminium, "Environmental profile report for the aluminium refining industry." *Tech. Rep. Bruxelles, Belgia* (2021).
5. D. Paraskevas, K. Kellens, W. Dewulf, and J. R. Duflou, *J. Cleaner Prod.*, **105**, 357 (2015).
6. S. H. Aschehoug, K. Øverbø Schulte, and M. M. Bjørnbet, *Proc. CIRP*, **57**, 734 (2016).
7. Towards Sustainable Cities Research Team, *Aluminium Recyclability and Recycling* (Nottingham, Llundain; UK)(Cwningen Press) (2015).
8. S. Tjøtta, L. Dardinier, and B. Kurth, *Alum. Extrus. Finish.* (2020), 18, http://www.aluminiumextrusion.it/2020-1-magazine.html.
9. S. Eggen, K. Sandaunet, L. Kolbeinsen, and A. Kvithyld, "Recycling of aluminium from mixed household waste." *Light Metals 2020*, ed. A. Tomsett (Cham, Switzerland)(Springer), 1091 (2020).
10. K. Al-Helal, J. Lazaro-Nebreda, J. B. Patel, and G. M. Scamans, *Recycling*, **6**, 66 (2021).
11. S. Tjøtta, L. Dardinier, G. Rombach, and R. Scharf-Bergmann, "Recycling end of life scrap into high-quality extrusion ingot." *Proceedings of the Twelfth International Aluminium Extrusion Technology Seminar & Exposition, MI39. Aluminum Extruders Council, Wauconda, IL, USA* (2022).
12. A. Lutz, M. Chojak Halseid, and I. De Graeve, *Mater. Corros.*, **73**, 1575 (2022).
13. V. K. Soo, J. Peeters, D. Paraskevas, P. Compston, M. Doolan, and J. R. Duflou, *J. Cleaner Prod.*, **178**, 119 (2018).
14. E. Senel and K. Nisancioglu, *Corros. Sci.*, **85**, 436 (2014).
15. E. Senel, J. C. Walmsley, S. Diplas, and K. Nisancioglu, *Corros. Sci.*, **85**, 167 (2014).
16. H. Kurt, S. Diplas, J. C. Walmsley, and K. Nisancioglu, *J. Electrochem. Soc.*, **160**, C542 (2013).
17. B. Graver, A. van Helvoort, J. C. Walmsley, and K. Nisancioglu, "Surface segregation of indium by heat treatment of aluminium." *Aluminium Alloys 2006 —ICAA10, Mater. Sci. Forum*, ed. W. Poole, M. Wells, and D. Lloyd (Trans Tech Publications) Vol. 519, p. 673 (2006).
18. G. Courval, J. Allin, G. Risto, and B. Costello, *Light Met. Age*, **68**, 35 (2010).
19. P. G. Sheasby, S. Wernick, and R. Pinner, *Surface Treatment and Finishing of Aluminum and Its Alloys* (Teddington, USA)(Finishing Publications) 5th ed. (1987).
20. I. Pires, L. Quintino, C. Rangel, G. Thompson, P. Sheldon, and X. Zhou, *Trans. IMF*, **68**, 179 (2000).
21. H. Shi, M. Yu, J. Liu, G. Rong, R. Du, J. Wang, and S. Li, *Corros. Sci.*, **169**, 108642 (2020).
22. Y. Ma, X. Zhou, G. Thompson, and P. Skeldon, *Corros. Sci.*, **66**, 292 (2013).
23. Z. Jin, C. Cai, T. Hashimoto, D. K. Yudie Yuan, J. Hunter, and X. Zhou, *J. Alloys Compd.*, **842**, 155834 (2020).
24. Z. Jin, C. Cai, T. Hashimoto, D. K. Yudie Yuan, J. Hunter, and X. Zhou, *Corros. Sci.*, **179**, 109134 (2021).
25. Z. Jin, C. Cai, Y. Yuan, D. Kang, J. Hunter, and X. Zhou, *Mater. Charact.*, **171**, 110768 (2021).
26. S. S. Golru, M. Attar, and B. Ramezanzadeh, *Prog. Org. Coat.*, **87**, 52 (2015).
27. F. J. Garcia-Garcia, E. V. Koroleva, G. E. Thompson, and G. C. Smith, *Surf. Interface Anal.*, **42**, 258 (2010).
28. I. Milošev et al., *J. Electrochem. Soc.*, **166**, C3131 (2019).
29. J. Qi, A. Němcová, J. Walton, X. Zhou, P. Skeldon, and G. Thompson, *Thin Solid Films*, **616**, 270 (2016).
30. A. S. Hamdy, I. Doench, and H. Möhwald, *J. Mater. Sci.*, **47**, 3784 (2012).
31. M. Li, S. Zanna, A. Seyeux, F. Wiame, P. Marcus, and J. Światowska, *J. Electrochem. Soc.*, **168**, 041504 (2021).
32. Y. Ma, X. Zhou, G. E. Thompson, X. Zhang, C. Luo, M. Curioni, and H. Liu, *J. Electrochem. Soc.*, **160**, C111 (2013).
33. H. Zhu, *JOM*, **66**, 2222 (2014).
34. S.-I. Pyun and S.-M. Moon, *J. Solid State Electrochem.*, **4**, 267 (2000).
35. E. Koroleva, G. Thompson, G. Hollrigl, and M. Bloeck, *Corros. Sci.*, **41**, 1475 (1999).
36. Yu, Z. Xiao, S. X Hao, and Q. S. Fu, *Adv. Mater. Res.*, **652-654**, 853 (2013).
37. F. Garcia-Garcia, P. Skeldon, G. Thompson, and G. Smith, *Electrochim. Acta*, **75**, 229 (2012).
38. M. Witkowska, G. E. Thompson, T. Hashimoto, and E. Koroleva, *Surf. Interface Anal.*, **45**, 1585 (2013).
39. S. W. Im, H. Ahn, D. H. Seo, S. Park, S. Choi, W. Ryu, K. Kim, E. S. Park, and K. T. Nam, *J. Mater. Chem. A*, **8**, 11133 (2020).
40. L. Feng, Y. Du, J. Huang, L. Cao, L. Feng, Y. Feng, Q. Liu, D. Yang, and K. Kajiyoshi, *Sustainable Energy Fuels*, **4**, 2850 (2020).
41. A. P. Sekhar, A. B. Mandal, and D. Das, *J. Mater. Res. Technol.*, **9**, 1005 (2020).
42. S. Kumari, S. Wenner, J. C. Walmsley, O. Lunder, and K. Nisancioglu, *J. Electrochem. Soc.*, **166**, C3114 (2019).
43. B. Holme, N. Ljones, A. Bakken, O. Lunder, J. E. Lein, L. Vines, T. Hauge, O. Bauger, and K. Nisancioglu, *J. Electrochem. Soc.*, **157**, C424 (2010).
44. A. Lutz, L. Lapeire, T. Nguyen-Minh, K. Verbeken, H. Terryn, and I. De Graeve, *Surf. Interface Anal.*, **51**, 1251 (2019).
45. A. Lutz, L. Malet, J. Dille, L. H. de Almeida, L. Lapeire, K. Verbeken, S. Godet, H. Terryn, and I. De Graeve, *J. Alloys Compd.*, **794**, 435 (2019).
46. M. Stern and A. L. Geary, *J. Electrochem. Soc.*, **104**, 56 (1957).
47. K. B. Oldham and F. Mansfeld, *Corros. Sci.*, **13**, 813 (1973).
48. E. Mysliu, K. Storli, E. Kjørsvik, O. Lunder, and A. Erbe, "Replication data for: Recycled aluminium alloys and their models: role and behaviour of alloying elements during alkaline etching." (2022), NTNU Open Research Data.
49. A. J. Bard and L. R. Faulkner, *Electrochemical Methods: Fundamentals and Applications* (New York)(Wiley) 2nd ed. (2001).
50. D. Chu and R. F. Savinell, *Electrochim. Acta*, **36**, 1631 (1991).
51. P. Deepa and R. Padmalatha, *Arabian J. Chem.*, **10**, S2234 (2017).
52. Y. Aleksandrov, E. Tsyganova, and A. Pisarev, *Russ. J. Gen. Chem.*, **73**, 689 (2003).
53. T. Hiraki, M. Takeuchi, M. Hisa, and T. Akiyama, *Mater. Trans.*, **46**, 1052 (2005).
54. A. Z. Zhuk, A. E. Sheindlin, B. V. Kleymenov, E. I. Shkolnikov, and M. Y. Lopatin, *J. Power Sources*, **157**, 921 (2006).
55. I. Boukerche, S. Djerad, L. Benmansour, L. Tifouti, and K. Saleh, *Corros. Sci.*, **78**, 343 (2014).
56. S. Abd El Wanees, S. Nooh, A. Farouk, and S. M Abd El Wanees, *J. Dispersion Sci. Technol.*, **43**, 2021 (2022).
57. J. Han, D. Thierry, and K. Ogle, *Corrosion*, **75**, 69 (2018).
58. M. R. Avei, M. Jafarian, H. M. B. Olyaei, F. Gobal, S. Hosseini, and M. Mahjani, *Mater. Chem. Phys.*, **143**, 0254 (2013).
59. C. M. A. Brett, *J. Appl. Electrochem.*, **20**, 1000 (1990).
60. C. M. Brett, *Corros. Sci.*, **33**, 1000 (1992).
61. H. Shao, J. Wang, Z. Zhang, J. Zhang, and C. Cao, *Mater. Chem. Phys.*, **77**, 0254 (2003).
62. A. Abdel-Gaber, E. Khamis, H. Abo-El Dahab, and S. Adeel, *Mater. Chem. Phys.*, **109**, 297 (2008).
63. P. R. Kumari, J. Nayak, and A. N. Shetty, *Arabian J. Chem.*, **9**, 1144 (2016).
64. K. Emregul and A. Aksüt, *Corros. Sci.*, **42**, 2051 (2000).
65. H.-J. Lee, I.-J. Park, S.-R. Choi, and J.-G. Kim, *J. Electrochem. Soc.*, **164**, A549 (2017).
66. Y. Wu, J. Xiong, R. Lai, X. Zhang, and Z. Guo, *J. Alloys Compd.*, **475**, 332 (2009).
67. L. Lodgaard and N. Ryum, *Mater. Sci. Eng. A*, **283**, 144 (2000).
68. Y. Birol, *Metall. Mater. Trans. A*, **44**, 504 (2013).
69. N. Kuijpers, W. Kool, P. Koenis, K. Nilsen, I. Todd, and S. van der Zwaag, *Mater. Charact.*, **49**, 409 (2002).
70. A. Afseth, J. Nordlien, G. Scamans, and K. Nisancioglu, *Corros. Sci.*, **43**, 2093 (2001).
71. G. Buytaert, H. Terryn, S. Van Gils, B. Kernig, B. Grzemba, and M. Mertens, *Surf. Interface Anal.*, **37**, 534 (2005).
72. E. P. Short and P. G. Sheasby, *Trans. IMF*, **47:1**, 27 (1969).
73. R. G. Buchheit, R. P. Grant, P. F. Hlava, B. Mckenzie, and G. L. Zender, *J. Electrochem. Soc.*, **144**, 2621 (1997).
74. R. G. Buchheit, M. A. Martinez, and L. P. Montes, *J. Electrochem. Soc.*, **147**, 119 (2000).
75. R. Buchheit, *Mater. Sci. Forum*, **331-337**, 1641 (2000).
76. B. B. M. Sultan, D. Thierry, J. Torrescano-Alvarez, and K. Ogle, *Electrochim. Acta*, **404**, 139737 (2022).
77. O. Gharbi, N. Birbilis, and K. Ogle, *J. Electrochem. Soc.*, **163**, C240 (2016).
78. O. Gharbi, N. Birbilis, and K. Ogle, *Electrochim. Acta*, **243**, 207 (2017).
79. M. Gentile, E. Koroleva, P. Skeldon, G. Thompson, P. Bailey, and T. Noakes, *Corros. Sci.*, **52**, 688 (2010).
80. M. Gentile, E. V. Koroleva, P. Skeldon, G. E. Thompson, P. Bailey, and T. C. Q. Noakes, *Surf. Interface Anal.*, **42**, 287 (2010).
81. H. Habazaki, M. Paez, K. Shimizu, P. Skeldon, G. Thompson, G. Wood, and X. Zhou, *Corros. Sci.*, **38**, 1033 (1996).
82. G. Frankel and D. Landolt, "Fundamentals of corrosion - kinetics of electrolytic corrosion reactions." *Encyclopedia of Electrochemistry*, ed. A. Bard, M. Stratmann, and G. Frankel (Weinheim, Germany)(Wiley-VCH) Vol. 4, Chap. 1, p. 1 (2003).
83. M. Doche, J. Rameau, R. Durand, and F. Novel-Cattin, *Corros. Sci.*, **41**, 805 (1999).
84. R. Brown and J. Whitley, *Electrochim. Acta*, **32**, 545 (1987).
85. A. K. Vijh, *J. Phys. Chem.*, **73**, 506 (1969).
86. J. Han, V. Vivier, and K. Ogle, *npj Mater. Degrad.*, **4**, 1 (2020).
87. A. Heuer, *J. Eur. Ceram. Soc.*, **28**, 1495 (2008).
88. U. Aschauer, P. Bowen, and S. Parker, *Acta Mater.*, **57**, 4765 (2009).
89. M Lechner, *Taschenbuch für Physiker und Chemiker. Band 1 - Physikalisch - chemische Daten* (Berlin)(Springer) (1992).
90. C. Tanford, *The Hydrophobic Effect: Formation of Micelles and Biological Membranes* (New York)(Wiley-Interscience) (1980).